



**IMAGE RECONSTRUCTION ALGORITHMS: UPDATE ON THE
ANALYSIS OF THE SCENE-DEPENDENT BIAS
SMOSP3-UPC-TN-0001 v 1.0**

**SMOSP3-UPC-TN-0001 v 1.0 Image Reconstruction Algorithms:
Update on the Analysis of the Scene-Dependent Bias**

Written by: A. Camps, M. Vall-llossera, I. Corbella, N. Duffo, F. Torres

Barcelona, 29 January 2007



Executive Summary

This TN is released in the frame of the task **L1P-UPC-T4 Define mitigation approaches for L1 Processing to compensate for the Scene Dependent Bias**, within the contract **UPC support to SMOS L1 Processor Prototype Phase 3.SMOSP3-UPC-PS-0001 v1.0 28th September 2006**. It is aimed to support DEIMOS in the implementation of the bias mitigation procedure in the L1 PPP3 processor.

This technical note includes the contents of a manuscript submitted to the IEEE Transactions on Geoscience and Remote Sensing (TGARS) on May 10th, 2006 on the Origin and Mitigation of the Scene-Dependent Bias. The study has been performed under the Spanish Research and EU Feder projects TEC2005-06863-C02-01/TCM and ESP2005-06823-C05-02.

This manuscript is now under the third review process and describes the two sources of Scene-Dependent Bias (SDB):

- Contributors to $T_A = V(0,0)$: NIR measurement errors, contributions from the back of the array, and imperfect cancellation of Sun (and to much lesser extent Moon), and
- Contributors to $V(u,v)$ (PMS and NIR measurement errors affecting the measurement of T_{sys} of each receiver (amplitude errors), differences between receivers' frequency responses (non-separable amplitude errors, and separable and non-separable phase errors) , errors in the estimation of the antenna solid angle (amplitude errors), non-zero antenna cross-polarization patterns (leakage between T_B images from different polarizations: image-dependent offset term), and offsets (although they produce biases that are not scene-dependent).

The SDB can be minimized by reducing the contrasts in the brightness temperature scene by adding all available information as proposed in previous versions of the image reconstruction algorithm, but also the land & iced-sea/sea mask and a reference ocean and a constant T_B over land to compute the differential visibilities to be inverted. In addition to a proposal, this algorithm has been implemented the SMOS End-to-end Performance Simulator (SEPS).



I. INTRODUCTION

The *MIRAS* instrument [1,2] is the single payload of the European Space Agency's *SMOS* mission, and it will be the first two-dimensional aperture synthesis radiometer for Earth observation. In aperture synthesis radiometers, the brightness temperature image reconstruction is performed through a Fourier synthesis process of the complex cross-correlations V_{12}^{pq} measured between the band pass signals $b_1(t)$ and $b_2(t)$ at “ p ” and “ q ” polarizations, collected by every pair of elements in the array, which is assumed to be located in the XY plane. According to [3,14] the samples of the visibility function are given by:

$$V_{12}^{pq}(u_{12}, v_{12}, w_{12} = 0) \stackrel{\Delta}{=} \frac{1}{k_B \sqrt{B_1 B_2} \sqrt{G_1 G_2}} \cdot \frac{1}{2} \langle b_1^p(t) b_2^{q*}(t) \rangle = \quad (1)$$

$$= \frac{1}{\sqrt{\Omega_1 \Omega_2}} \iint_{\xi^2 + \eta^2 \leq 1} \frac{(T_{pq}(\xi, \eta) - T_{rec} \delta_{pq})}{\sqrt{1 - \xi^2 - \eta^2}} F_{n,p1}(\xi, \eta) F_{n,q2}^*(\xi, \eta) \tilde{r}_{12} \left(-\frac{u_{12}\xi + v_{12}\eta}{f_0} \right) \exp(-j2\pi(u_{12}\xi + v_{12}\eta)) d\xi d\eta,$$

where k_B is the Boltzmann's constant, $B_{1,2}$ and $G_{1,2}$ are the receivers' noise bandwidth and power gain, $\Omega_{1,2}$ is the solid angle of the antennas, $T_{pq}(\xi, \eta)$ is the brightness temperature (T_B) of the scene, T_{rec} is the physical temperature of the receivers (the so-called “Corbella term”), $\delta_{pq}=1$ if $p=q$ and 0 if $p \neq q$, $F_{n,p,q}(\xi, \eta)$ are the normalized antenna co-polar voltage patterns (amplitude and phase) at “ p ” and “ q ” polarizations, $\tilde{r}_{12}(-\frac{u_{12}\xi + v_{12}\eta}{f_0})$ is the so-called fringe-washing function that accounts for spatial decorrelation effects and depends on the frequency response of the pair of elements collecting the signals being correlated, (u_{12}, v_{12}, w_{12}) is the spatial frequency (baseline) that depends on the antenna position difference: $(u_{12}, v_{12}, w_{12}) = (x_2 - x_1, y_2 - y_1, z_2 - z_1) / \lambda_0$ (in this case $z_1 = z_2$ and $w_{12} = 0$), $\lambda_0 = c/f_0$ is the wavelength and f_0 is the central frequency of the receivers, and the director cosines $(\xi, \eta) = (\sin \theta \cos \phi, \sin \theta \sin \phi)$ are defined with respect to the X and Y axes.

In the ideal case, when all the antenna patterns are equal ($F_{n,p1}(\xi, \eta) = F_{n,q2}(\xi, \eta) = F_n(\xi, \eta)$ and $\Omega_1 = \Omega_2 = \Omega$), spatial decorrelation effects are negligible ($\tilde{r}_{12} \approx 1$), and there are not antenna position errors (the (u, v) points are equal to their nominal values), the relationship between the so called modified brightness temperature $\bar{T}(\xi, \eta)$ (by definition the term within the brackets in (2)) and the visibility function reduces to a Fourier transform relationship that is then sampled at the specific baselines determined by the antenna positions in the array:

$$V_{12}^{pq}(u_{12}, v_{12}) = F \left[\frac{(T_{pq}(\xi, \eta) - T_{rec} \delta_{pq}) |F_n(\xi, \eta)|^2}{\sqrt{1 - \xi^2 - \eta^2} \Omega} \right]. \quad (2)$$

Since the support of the T_B to be retrieved is the unit circle $\xi^2 + \eta^2 \leq 1$, it is known that the optimum sampling strategy of the (u, v) plane is on a hexagonal grid, instead of the usual rectangular one. This sampling strategy allows one to increase the maximum antenna separation from $d = \lambda_0/2$ to $d = \lambda_0/\sqrt{3}$, and still not suffer from aliasing effects in the image reconstruction process. In addition, if the (ξ, η) points in which the T_B is being reconstructed¹ are properly selected, the hexagonally sampled visibility function can be processed with standard (rectangular) fast Fourier Transform (FFT) algorithms [4,5].

For a given number of elements, the array structure that provides an hexagonal sampling of the (u, v) plane and the largest (u, v) coverage (the best angular resolution) is a Y structure, which is the shape of the *MIRAS* instrument (Fig. 1).



Figure 1. SMOS artist view with the three arms deployed forming a Y-shaped structure. The total number of receiving elements in the interferometric radiometer is 69 (image courtesy of ESA Medialab).

However, in *MIRAS*, after an optimization process of the swath width, the revisit time, the angular resolution, and the range of incidence angles over the Earth that are imaged, it was decided to increase even more the antenna spacing from $d = \lambda_0/\sqrt{3}$ to $d = 0.89\lambda_0$ first, and it was modified later to $d = 0.875\lambda_0$, which is the current value (Fig. 2) [7].

¹ SMOS has two modes of operation: dual-polarization and full-polarimetric [6]. In the dual-polarization mode a complete T_B image can be formed at a given polarization after each integration time. In the full-polarimetric mode a 4 step switching sequence is required and only after 4 basic periods a set of T_B images (4 Stokes elements) can be formed.

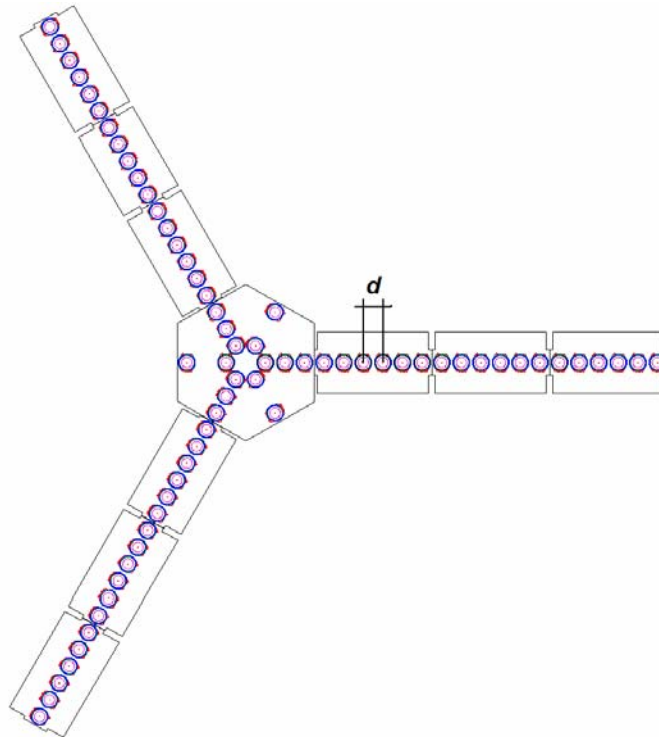


Figure 2. SMOS Y-shaped array composed by 3 x 23 elements (15 in the hub, and 6 in each section of the arms).
Element spacing d is $0.875 \lambda_0$.

Since $d = 0.875 \lambda_0 > \lambda_0 / \sqrt{3}$, the closest six replicas of the T_B supported by the unit circle overlap with the main one, and there is “aliasing.” The alias-free field of view (AF-FOV) limited by the periodic repetition of the unit circle is in fact very small (gray region in Fig. 3). However, since a significant part of the aliases correspond to the cold and known sky, the AF-FOV can be extended (E-AF-FOV) up to the region limited by the periodic repetition of the Earth’s disk [4,5] (Fig. 3, gray region).

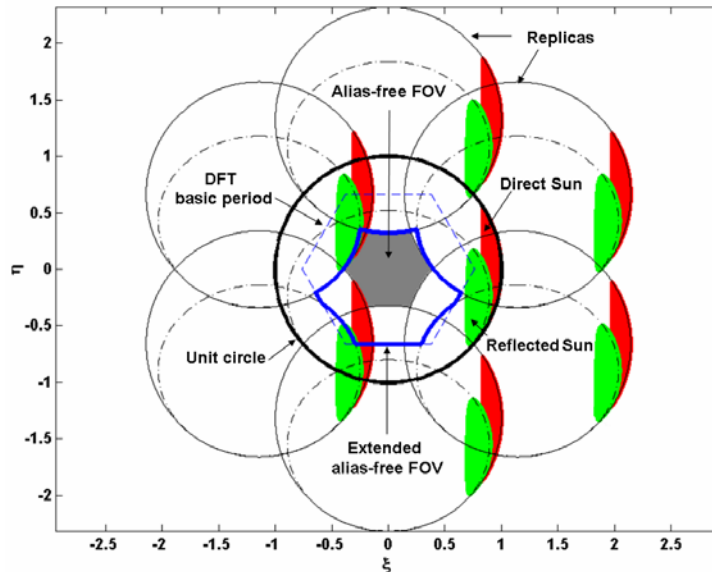


Figure 3. Aliasing in 2D aperture synthesis Y-shaped interferometric radiometers for an antenna spacing of 0.875 wavelengths, 32° array tilt, 30° array steering and 755 km platform height. Representation of the Earth's disk (Earth-sky horizon), unit circle, DFT basic period, geometric place of the Sun positions (direct and reflected images), and their six closest replicas to the main DFT period (from [16]).

Despite this improvement, the limited angular resolution of the instrument, and the large T_B step at the Earth aliases border introduced a significant ringing (Gibbs phenomenon) and slightly reduced the true extension of the E-AF-FOV. To mitigate this effect, it was also proposed [4,8] to subtract a contribution from a fictitious constant T_B Earth disk, determined in such a way that the residual visibilities (ΔV : differential visibilities) to be inverted lead to a zero mean T_B image ($\Delta V(0,0)=0$).

In addition to the extension of the AF-FOV, these improvements (subtraction of the sky and a constant T_B Earth), reduced the impact of systematic errors in the image reconstruction process, while at the same time accelerated the convergence of the image reconstruction process. However, when comparing the reconstructed T_B images (limited to the AF-FOV or to the E-AF-FOV) with the original ones used as inputs to test the algorithms, there is a bias (mean of the difference between the original and retrieved T_B images in the AF-FOV), which is found not to be constant, but dependent on the T_B scene being imaged. This bias is larger for T_B scenes with large contrasts, and smaller for more homogeneous T_B scenes.

II. UNDERSTANDING THE ORIGIN OF THE SCENE-DEPENDENT BIAS

II.1. One-dimensional Fourier Transform case

In order to understand the origin of the scene-dependent bias, a simple and clarifying example is analyzed in the one dimensional case using only discrete Fourier transforms of even and odd functions. Any even/odd function within the fundamental period $[-1, 1]$ can be expanded as a Fourier series as in (3a) or (3d), respectively. The presence of amplitude errors in the Fourier components $n \neq 0$ in an even/odd function produces an error function which is also even/odd, (3b) and (3e) and whose mean value computed in the whole $[-1, 1]$ period is zero.

$$f(\xi) = \sum_n a_n \cos(n\pi\xi) \quad (3a)$$

$$f(\xi) = \sum_n a_n (1 + \Delta a_n) \cos(n\pi\xi) = \sum_n a_n \cos(n\pi\xi) + \sum_n \Delta a_n \cdot a_n \cos(n\pi\xi) \quad (3b)$$

$$f(\xi) = \sum_n a_n \cos(n\pi\xi + \Delta\phi_n) = \sum_n a_n \cos(n\pi\xi) \cos(\Delta\phi_n) - \sum_n a_n \sin(n\pi\xi) \sin(\Delta\phi_n) \approx \sum_n a_n \cos(n\pi\xi) - \sum_n \Delta\phi_n \cdot a_n \sin(n\pi\xi) \quad (3c)$$

$$f(\xi) = \sum_n b_n \sin(n\pi\xi) \quad (3d)$$

$$f(\xi) = \sum_n b_n (1 + \Delta b_n) \sin(n\pi\xi) = \sum_n b_n \sin(n\pi\xi) + \sum_n \Delta b_n \cdot b_n \sin(n\pi\xi) \quad (3e)$$

$$f(\xi) = \sum_n b_n \sin(n\pi\xi + \Delta\phi_n) = \sum_n b_n \sin(n\pi\xi) \cos(\Delta\phi_n) + \sum_n b_n \cos(n\pi\xi) \sin(\Delta\phi_n) \approx \sum_n b_n \sin(n\pi\xi) + \sum_n \Delta\phi_n \cdot b_n \cos(n\pi\xi) \quad (3f)$$

However, as it can be readily demonstrated from (3b) and (3e), for any other symmetric interval² $[-\xi_0, \xi_0]$ the mean value of the error function is not zero for even functions (3b), while it is zero for odd functions (3e). The magnitude of this non-zero bias depends on the magnitude of the errors themselves (Δa_n) and on the spectral components of the image to be reconstructed (a_n).

Conversely, the presence of small phase errors in the Fourier components $n \neq 0$ in an even/odd function produces an error function which is now odd/even, (3c) and (3f) and whose mean value computed in the whole $[-1, 1]$ period is also zero. However, as it can be readily demonstrated from (3c) and (3f), for any other symmetric interval $[-\xi_0, \xi_0]$ it is zero for even functions (3c), while it is not zero for odd functions (3f). The magnitude of this non-zero bias also depends on the magnitude of the errors themselves ($\Delta\phi_n$) and on the spectral components of the image to be reconstructed (b_n).

Similarly, offset errors in a_n or b_n also induce even or odd error functions, as in eqns. (3b) and (3e), respectively.

² Typical sensor configurations have a symmetric field-of-view around boresight. For non-symmetric intervals, both amplitude and phase errors do contribute simultaneously to the bias of even or odd functions.

These biases are what have been called the Scene-Dependent Bias (SDB) and the above discussion explains why the SDB encountered were higher for non-homogeneous T_B scenes (larger a_n components). In general, any function could be decomposed into an even and odd functions: $f_{even}(\xi) = (f(\xi) + f(-\xi))/2$ and $f_{odd}(\xi) = (f(\xi) - f(-\xi))/2$ and the total SDB will be the sum of the SDB due to amplitude error contributions on $f_{even}(\xi)$ and the SDB due to phase error contributions on $f_{odd}(\xi)$.

When considering the whole period $[-1, 1]$ neither amplitude, nor phase errors in the Fourier coefficients introduce a bias, although they do impact the rms error. Only errors in zero-frequency Fourier coefficient a_0 induce a bias, which is obviously the same regardless of the subinterval $[\xi_1, \xi_2]$ considered.

To illustrate these effects fig. 4 shows the impact of 3% amplitude (center) and 3° phase (right) errors on the Fourier series reconstruction of even (top) and odd (bottom) pulse functions. Ideal reconstruction is shown on the left. Computed biases for the $[-1,1]$ and $[-1/3, +1/3]$ intervals are given in the figure. As it can be appreciated, amplitude and small phase errors are of multiplicative nature and produce zero bias in the $[-1, 1]$ interval, but a non-zero bias on the even and odd functions, respectively.

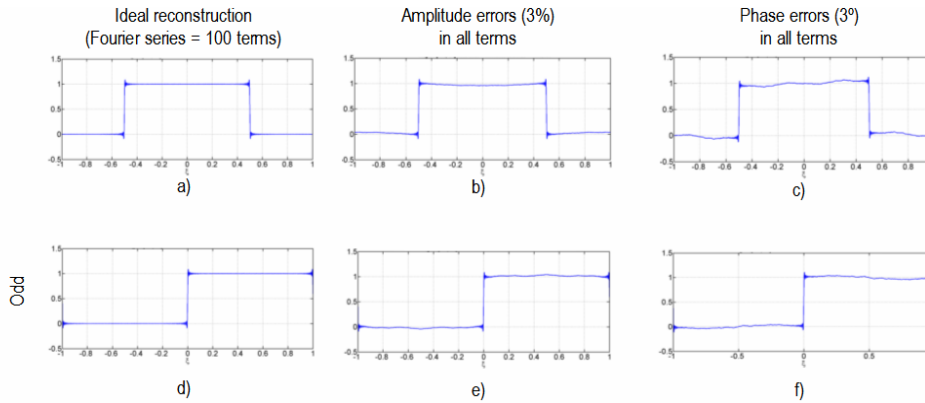


Figure 4. Impact of amplitude (center) and phase (right) errors on the Fourier series reconstruction of even (top) and odd (bottom) functions. Ideal reconstruction is shown on the left. Amplitude and small phase errors are of multiplicative nature.

- a) Region $[-1.0, 1.0]$: rms error = 0.023 bias = $-5.0 \cdot 10^{-4}$; Region $[-1/3, 1/3]$: rms error = 0.001 bias = $-1.2 \cdot 10^{-5}$
- b) Region $[-1.0, 1.0]$: rms error = 0.036 bias = $-4.8 \cdot 10^{-4}$; Region $[-1/3, 1/3]$: rms error = 0.007 bias = $-3.2 \cdot 10^{-2}$
- c) Region $[-1.0, 1.0]$: rms error = 0.045 bias = $-5.0 \cdot 10^{-4}$; Region $[-1/3, 1/3]$: rms error = 0.033 bias = $-1.4 \cdot 10^{-3}$
- d) Region $[-1.0, 1.0]$: rms error = 0.026 bias = $-2.5 \cdot 10^{-4}$; Region $[-1/3, 1/3]$: rms error = 0.028 bias = $-7.5 \cdot 10^{-4}$
- e) Region $[-1.0, 1.0]$: rms error = 0.032 bias = $-2.5 \cdot 10^{-4}$; Region $[-1/3, 1/3]$: rms error = 0.031 bias = $-7.5 \cdot 10^{-4}$
- f) Region $[-1.0, 1.0]$: rms error = 0.036 bias = $-2.6 \cdot 10^{-4}$; Region $[-1/3, 1/3]$: rms error = 0.030 bias = $2.7 \cdot 10^{-2}$

II.2. Two-dimensional Fourier Transform case



In the two-dimensional case of the MIRAS instrument, the Y-shaped array leads to samples of the visibility function $V_{m,n}^{pq}(u_{m,n}, v_{m,n})$ over a hexagonal $(u_{m,n}, v_{m,n})$ grid. The visibility function (eqn. (1)) is usually expressed in terms of the module and phase as $|V_{m,n}^{pq}(u_{m,n}, v_{m,n})| \cdot \exp(j\phi_{V(u_{m,n}, v_{m,n})}) \square |V_{m,n}| \cdot \exp(j\phi_{m,n})$. Then, in the ideal case, the reconstruction of the modified brightness temperature $\bar{T}(\xi, \eta)$ can then be computed from a DFT [4,5]:

$$\begin{aligned} \bar{T}(\xi, \eta) &\stackrel{\Delta}{=} \frac{\sqrt{3} d^2}{2} \sum_m \sum_n |V_{m,n}| \exp(j\phi_{m,n}) \exp(j2\pi(u_{m,n}\xi + v_{m,n}\eta)) = \\ &= \frac{\sqrt{3} d^2}{2} \sum_m \sum_n \left\{ |V_{m,n}| \cos(\phi_{m,n}) \cos(j2\pi(u_{m,n}\xi + v_{m,n}\eta)) - |V_{m,n}| \sin(\phi_{m,n}) \sin(j2\pi(u_{m,n}\xi + v_{m,n}\eta)) \right\} = \\ &= \frac{\sqrt{3} d^2}{2} \sum_m \sum_n \left\{ a_{m,n} \cos(j2\pi(u_{m,n}\xi + v_{m,n}\eta)) + b_{m,n} \sin(j2\pi(u_{m,n}\xi + v_{m,n}\eta)) \right\}, \end{aligned} \quad (4a)$$

where in eqn (4a) we have used the fact that $\bar{T}(\xi, \eta)$ is real and the visibility samples are hermitian.

Amplitude ($\hat{V}_{m,n} = |V_{m,n}| \cdot (1 + \Delta|V_{m,n}|) \cdot \exp(j\phi_{m,n})$) and phase ($\hat{V}_{m,n} = |V_{m,n}| \cdot \exp(j(\phi_{m,n} + \Delta\phi_{m,n}))$) errors in the visibility samples then translate into errors in the modified brightness temperature:

$$\Delta\bar{T}(\xi, \eta) \stackrel{\Delta}{=} \frac{\sqrt{3} d^2}{2} \sum_m \sum_n \Delta|V_{m,n}| \cdot \left\{ a_{m,n} \cos(j2\pi(u_{m,n}\xi + v_{m,n}\eta)) + b_{m,n} \sin(j2\pi(u_{m,n}\xi + v_{m,n}\eta)) \right\}, \quad (4b)$$

$$\Delta\bar{T}(\xi, \eta) \stackrel{\Delta}{=} \frac{\sqrt{3} d^2}{2} \sum_m \sum_n \Delta\phi_{m,n} \cdot \left\{ b_{m,n} \cos(j2\pi(u_{m,n}\xi + v_{m,n}\eta)) - a_{m,n} \sin(j2\pi(u_{m,n}\xi + v_{m,n}\eta)) \right\}. \quad (4c)$$

Note that eqn. (4b) is equivalent to the sum of (3b) and (3e) and eqn. (4c) is equivalent to the sum of (3c) and (3f). Offset errors in the complex visibility samples create a similar effect as in the 1D case.

As explained in the introduction, in this case the bias is computed as the mean of the difference between the original and the retrieved T_B images in the AF-FOV, which is determined by the inner region determined by six circles with radius equal to 1 and centers located at $\frac{2}{\sqrt{3}d} \cdot \left(\cos\left(\frac{\pi}{3} \cdot n + \frac{\pi}{6}\right), \sin\left(\frac{\pi}{3} \cdot n + \frac{\pi}{6}\right) \right); n = 0 \dots 5$, which depend on the antenna spacing d .

The above results show that the problem of the SDB is a general to one- and two-dimensional aperture synthesis radiometers imaging under aliasing conditions, or when the field-of-view is restricted to a fraction of the fundamental interval.

II.3. Two-dimensional Case: MIRAS Error Model and Sources of SDB

The *MIRAS* error model is summarized in eqn. (5) below:

$$\begin{aligned} \begin{bmatrix} \mu_{12r}^{pq} \\ \mu_{12j}^{pq} \end{bmatrix} &= \frac{1}{\sqrt{\langle |b_1^p|^2 \rangle} \sqrt{\langle |b_2^q|^2 \rangle}} \begin{bmatrix} \Re \\ \Im \end{bmatrix} \left\{ \langle b_1^p b_2^{q*} \rangle \right\} = \frac{1}{\sqrt{\langle |b_1^p|^2 \rangle} \sqrt{\langle |b_2^q|^2 \rangle}} \begin{bmatrix} \langle i_1^p i_2^q \rangle \\ \langle q_1^p i_2^q \rangle \end{bmatrix} = g_1 g_2 \begin{bmatrix} \Re \\ \Im \end{bmatrix} \left\{ V_{12}^{pq} \right\} = \\ &= g_1 g_2 \left\{ \begin{array}{l} \tilde{r}_{i_1^p i_2^q}(0) \\ \tilde{r}_{q_1^p i_2^q}(0) \end{array} \right\} \frac{1}{\sqrt{\Omega_1 \Omega_2}} \cdot \begin{bmatrix} \Re \\ \Im \end{bmatrix} \left\{ \iint_{\xi^2 + \eta^2 \leq 1} \frac{(T_{pq}(\xi, \eta) - T_{rec} \delta_{pq}) F_{n1}(\xi, \eta) F_{n2}^*(\xi, \eta)}{\sqrt{1 - \xi^2 - \eta^2}} \begin{bmatrix} \tilde{r}_{n i_1^p i_2^q}(\tau) \\ \tilde{r}_{n q_1^p i_2^q}(\tau) \end{bmatrix} e^{-j 2\pi (u_{12} \xi + v_{12} \eta + w_{12} \sqrt{1 - \xi^2 - \eta^2})} d\xi d\eta \right\} + \begin{bmatrix} \mu_{12,roff} \\ \mu_{12,joff} \end{bmatrix} \end{aligned} \quad (5)$$

where:

- The 1 bit/2 level digital correlators' output μ_{12r}^{pq} and μ_{12j}^{pq} are the real and imaginary parts of the normalized visibility samples, which are computed from the in-phase (*i*) and quadrature (*q*) components, at "p" and "q" polarizations.
- The amplitude factors $g_{1,2} = \sqrt{1/T_{sys\ 1,2}}$, being $T_{sys\ n}$ the system temperature of the *n*th channel, are due to the use of 1 bit/2 level digital correlators in *MIRAS*. An error in the estimation of the system temperatures $\hat{T}_{sys\ n} = T_{sys\ n} + \Delta T_{sys\ n}$ leads to an amplitude error $\hat{g}_n = g_n + \Delta g_n$.
- The fringe-washing function at the origin ($\tilde{r}_{i_1^p i_2^q}(0)$ or $\tilde{r}_{q_1^p i_2^q}(0)$) contains the separable (θ_1, θ_2) and non-separable (θ_{12}) phase errors, and the non-separable amplitude errors (g_{12}). The quadrature errors appear due to the different frequency responses between the I and Q channels.
- The antenna radiation voltage patterns (cross-polar patterns not included for simplicity, see Appendix 1, eqn. A.2) induce errors that are function of the (ξ, η) direction and can only be compensated in the image reconstruction process. The antenna solid angles $\Omega_{1,2}$ induce an amplitude error.
- The normalized fringe-washing function:

$$\tilde{r}_{n i_1^p i_2^q}(\tau) = \frac{\tilde{r}_{i_1^p i_2^q}(\tau)}{\tilde{r}_{i_1^p i_2^q}(0)}, \quad (6a)$$

$$\tau = - \frac{u_{12} \xi + v_{12} \eta + w_{12} \sqrt{1 - \xi^2 - \eta^2}}{f_0}, \quad (6b)$$

provides the shape of the spatial decorrelation for each baseline and for each direction (eqn. (6b))



- The *antenna position errors* induce baseline errors $(\Delta u_{12}, \Delta v_{12}, \Delta w_{12})$ that lead to non-separable and direction-dependent errors $\exp\left(-j2\pi\left(\Delta u_{12}\xi + \Delta v_{12}\eta + \Delta w_{12}\sqrt{1-\xi^2-\eta^2}\right)\right)$ that can only be compensated in the image reconstruction process.
- And the *offset errors* which are due to leakage of the local oscillator, *sampling errors of the analog-to-digital converters...* These errors are constant for each baseline, but random from baseline to baseline, appear as “constant” noise in the T_B image (do not average out).

From the MIRAS error sources listed in the model described above the following sources of SDB can be readily identified as contributors to the zero-baseline, as amplitude or phase errors, or as image-dependent offset terms:

Sources affecting $T_A = V(0,0)$:

- Noise Injection Radiometer (NIR) measurement errors (finite sensitivity, bias ...),
- contributions to the antenna temperature coming from the back of the array (fore and aft images), and
- imperfect cancellation of Sun (and to much lesser extent Moon) contribution to T_A measured by the NIR

Sources affecting $V(u,v) \neq V(0,0)$:

- PMS and NIR errors affecting measurement of T_{sys} of each receiver ($g_{1,2}$: separable amplitude error),
- differences between receivers frequency responses (g_{12} : non-separable amplitude error, and $\theta_{1,2}, \theta_{12}$ separable and non-separable phase errors),
- errors in the antenna pattern measurement leading to inaccurate antenna solid angle estimations ($\Omega_{1,2}$), and
- non-zero antenna cross-polarization patterns which produces a leakage between brightness temperature images from different polarizations (image-dependent offset term).

III. Mitigating the Scene-Dependent Bias: Improvement of the Image Reconstruction Algorithm

In section II it was shown that amplitude and phase errors appear as multiplicative errors of the spectral components. Therefore, the minimization of the contrast of the T_B scene to be reconstructed will reduce the amplitude of the higher spectral components, and so the impact of these errors. The idea to achieve this goal is quite simple and can be considered an extension and improvement of previous versions of the image reconstruction algorithm [4, 8, 16]. In addition to the “a priori” information already used to pre-process the visibility samples (sky horizon, sky T_B map, estimated T_B from the Sun and Moon; see Appendix 1, sections A and B), the land/sea mask is used to computed the visibilities corresponding to a reference ocean

brightness temperature (computed with the following parameters 35 psu, 15°C and 4 m/s, although their choice is not critical since the brightness temperature of the sea changes very little with respect to them, and also the variations of T_B over land are much larger), and a constant T_B over land and over the iced sea (to be determined, eqn. 8), that will be subtracted from the calibrated visibilities prior to inversion.

The differential visibilities can then be computed as:

$$\begin{aligned} \Delta V^{pq}(u, v) = & V^{pq}(u, v) - V_R^{pq}(u, v) - V_{sky}^{pq}(u, v) - V_{sea}^{pq}(u, v) - T_{land}^{pq} \bar{V}_{land}^{pq}(u, v) \\ & - T_{Sun,dir}^{pq} \bar{V}_{Sun,dir}^{pq}(u, v) - T_{Sun,dir} \bar{V}_{Sun,scatt}^{pq}(u, v) - T_{Moon,dir} \bar{V}_{Moon,dir}^{pq}(u, v) \\ & - T_{Moon,dir} \bar{V}_{Moon,scatt}^{pq}(u, v) - V_{back}^{pq}(u, v), \end{aligned} \quad (7)$$

where T_{land}^{pq} is the value of the mean T_B over the land and iced sea regions, which have a high T_B value, similar to dry soil. With the appropriate value of T_{land}^{pq} :

$$\begin{aligned} T_{land}^{pq} \overset{\Delta}{=} & \left\{ \bar{T}_A^{pq} - V_{sky}^{pq}(0,0) - V_{sea}^{pq}(0,0) - V_{back}^{pq}(0,0) - T_{Sun,dir}^{pq} \bar{V}_{Sun,dir}^{pq}(u, v) \right. \\ & - T_{Sun,dir} \bar{V}_{Sun,scatt}^{pq}(0,0) - T_{Moon,dir} \bar{V}_{Moon,dir}^{pq}(0,0) \\ & \left. - T_{Moon,dir} \bar{V}_{Moon,scatt}^{pq}(0,0) \right\} / \bar{V}_{land}^{pq}(0,0), \end{aligned} \quad (8)$$

then $\Delta V^{pq}(0,0) = 0$ and the image obtained from eqn. (7) has zero-mean. Note that in (7) the Corbella term is not present since it exists only in baselines formed by two different receivers. In *MIRAS* the zeroth baseline is measured by three different Noise Injection Radiometers (NIRs) (eqn. (A.5)). In eqn. (7), \bar{V}_{land}^{pq} and V_{sea}^{pq} are computed as:

$$\begin{aligned} \bar{V}_{land}^{pq} \overset{\Delta}{=} & \frac{1}{\sqrt{\Omega_1 \Omega_2}} \iint_{\xi^2 + \eta^2 \leq \text{land or iced sea}} \frac{1}{\sqrt{1 - \xi^2 - \eta^2}} \hat{F}_{n1}^p(\xi, \eta) \hat{F}_{n2}^{q*}(\xi, \eta) \hat{r}_{12} \left(-\frac{u_{12}\xi + v_{12}\eta + w_{12}\sqrt{1 - \xi^2 - \eta^2}}{f_0} \right) \\ & \exp\left(-j2\pi(u_{12}\xi + v_{12}\eta + w_{12}\sqrt{1 - \xi^2 - \eta^2})\right) d\xi d\eta, \end{aligned} \quad (9)$$

$$\begin{aligned} V_{sea}^{pq} \overset{\Delta}{=} & \frac{1}{\sqrt{\Omega_1 \Omega_2}} \iint_{\xi^2 + \eta^2 \leq \text{sea}} \frac{T_{B,sea}(\xi, \eta)}{\sqrt{1 - \xi^2 - \eta^2}} \hat{F}_{n1}^p(\xi, \eta) \hat{F}_{n2}^{q*}(\xi, \eta) \hat{r}_{12} \left(-\frac{u_{12}\xi + v_{12}\eta + w_{12}\sqrt{1 - \xi^2 - \eta^2}}{f_0} \right) \\ & \exp\left(-j2\pi(u_{12}\xi + v_{12}\eta + w_{12}\sqrt{1 - \xi^2 - \eta^2})\right) d\xi d\eta, \end{aligned} \quad (10)$$

where $T_{B,sea}(\xi, \eta)$ is the brightness temperature of the reference sea.



Note that in previous versions of the proposed image reconstruction algorithm instead of $V_{sea}^{pq}(u,v) + T_{land}^{pq} \bar{V}_{land}(u,v)$ in (4) a constant T_B was subtracted within the Earth's disk: $T_{Earth}^{pq} \bar{V}_{Earth}(u,v)$ (see [4] or [8] for more details). This decomposition significantly reduced the Gibbs phenomenon (ringing) near the Earth aliases and accelerated the convergence towards the solution of iterative methods. The decomposition of the T_B within the Earth's disk into these two terms ocean and land/iced sea, reduces even further the high frequency contents of the T_B image to be reconstructed, thus improving the convergence and minimizing the impact of errors, and the SDB.

After the image reconstruction process (determining $\Delta T_B^{pq}(\xi,\eta)$ from $\Delta V^{pq}(u,v)$ (eqn. 7), see Appendix 1), the total T_B image is formed by adding the ΔT , the sea and the land/iced sea contributions:

$$T_B^{pq}(\xi,\eta) \triangleq \Delta T_B^{pq}(\xi,\eta) + T_{sea}^{pq}(\xi,\eta) + T_{land}^{pq} \cdot land(\xi,\eta) \quad , \quad (11)$$

where $land(\xi,\eta)$ is a function that defines the (ξ,η) region occupied by land or iced sea. The brightness temperature of the iced sea is very high, similar or even higher than that of dry soil. The function $land(\xi,\eta)$ is derived from coastline and inner water bodies maps and the MIRAS instrument position and attitude.

IV. SIMULATION RESULTS

The simulation strategy that has been followed consist of simulating the MIRAS instrument as close to reality as possible (as in SEPS 4.0 release, February 1st, 2006), and from the potential effects listed in section I, the Sun is "turned off" and the antenna back lobes have not been simulated. All other instrument imperfections have been accounted for, including the thermal noise due to finite integration time, but in order to make a fair inter-comparison of the results, the random numbers generator has always been initialized with the same seed, so the simulation results are repetitive and show only the effects associated to the structure of the image under study.

Figure 5 left shows the original brightness temperature image used in the first snap-shot for testing the algorithms. Figure 5 center shows the reconstructed brightness temperatures by an ideal instrument (no errors at all) in which the image reconstruction is performed by an inverse hexagonal FFT only, without the application of the visibility decomposition described above. It is evident that without the visibility decomposition, the AF-FOV is mainly limited by the periodic repetition of the Earth replicas (the sky contribution is much smaller). Figure 5 right shows the reconstructed brightness temperature for an instrument with error using the visibility decomposition proposed. In this case, the support of the reconstructed can be enlarged even beyond the nominal extended AF-FOV (Fig. 3). In fact, it is no longer limited by the periodic

repetition of the Earth aliases (Fig. 5 center), but by the periodic repetition of the land regions (Fig. 5, right), and where there are ocean aliases overlapping with land the errors are small.

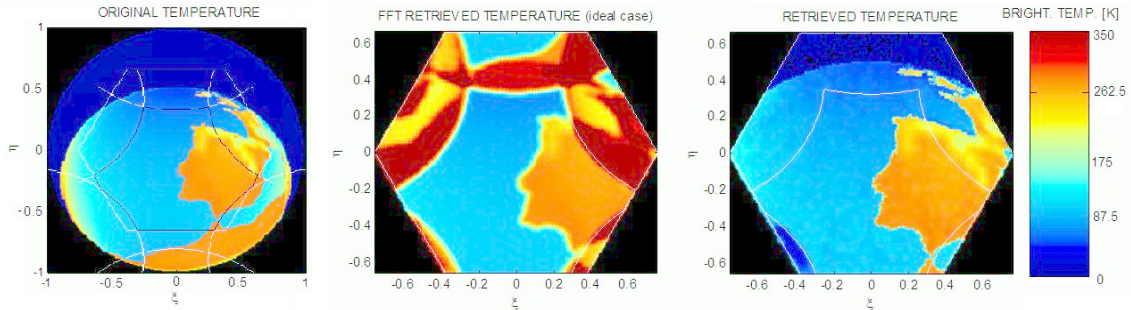


Figure 5. First snap-shot of the series. Left: original T_B image, fundamental (ξ, η) hexagonal period (white) and AF-FOV as limited by the periodic repetition of Earth replicas (black). Center: retrieved T_B image by an ideal system ($F_n = 1$, $\tilde{r} = 1$, and no antenna position errors). Right: retrieved T_B image for an instrument with errors after applying the visibility decomposition.

Figure 6 left shows the error T_B image between Fig. 5 center (FFT reconstructed image by an ideal instrument: $F_{n,p1}(\xi, \eta) = F_{n,q2}(\xi, \eta) = F_n(\xi, \eta) = 1$ and $\Omega_1 = \Omega_2 = \Omega$, negligible spatial decorrelation effects $\tilde{r}_{12} \approx 1$, and no antenna position errors) and the original image (Fig. 5 left). Figure 6 right shows the error T_B image between Fig. 5 right (retrieved image with a system including all the different error sources, except for the Sun and the antenna backlobes that have not been included) and the original image (Fig. 5 left). As compared to Fig. 5 center (ideal case, but no visibility decomposition) the field of view has been extended and also the errors are relatively small in the reconstructed image when ocean aliases overlap with land in the main image (e.g. North East of Spain and France: blue circle) and a larger error when land aliases overlap with sea in the main image (e.g. France over the lower left corner of the hexagon, and Spain in the upper left side of the hexagon: red circles). Note also that the width of the coastline is significantly reduced, which may be used to improve the retrieval of sea salinity and soil moisture close to the coastlines.

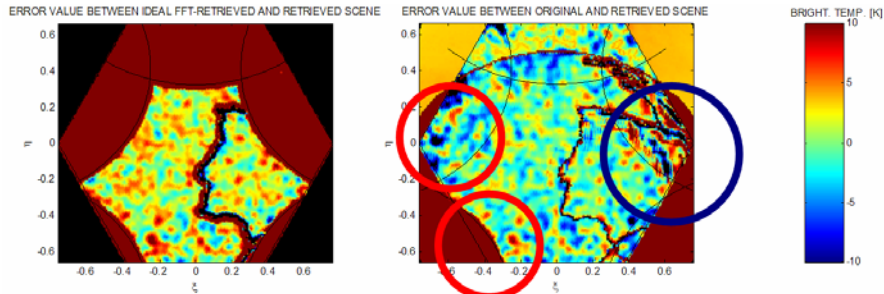


Figure 6. Left: error between the T_B image retrieved by an ideal system and the original one. Right: error between the T_B retrieved image for an instrument with errors after applying the visibility decomposition and the original one. Error is reduced in the coastlines and even in the alias regions circled. Color scale truncated for contrast enhancement.

Finally, Fig. 7 shows the evolution of the bias and rms error of the error T_B images computed from the difference image between the retrieved and the original ones, in the AF-FOV (not the extended AF-FOV) with a margin equal to the grid spacing in which the image reconstruction has been performed ($N_T=256$, instead of the minimum $N_{Tmin}=64$): $2/(\sqrt{3}N_T d) = 0.0052$ (about 14% of the actual pixel's size) to minimize any aliases spill over. In abscisas it is indicated the snap-shot number (each pair of H- and V- polarizations are simulated to be acquired with a time interval of 180 s). As already commented, all instrument parameters correspond to the default ones in the latest release of SEPS 4.0 (February 1st, 2006). As it can be appreciated, the bias is nearly cancelled except in snap-shots 11 to 13 when there are no coastlines, even in the aliased regions. In these cases, the scene is very smooth and the biases are mainly introduced by NIR errors and antenna cross-polarization errors that cannot be compensated using this technique. In this situation, the technique described in [9] is more suitable, although it is applied to the final T_B maps, and not prior or during the image reconstruction process. The apparently high rms errors in snap-shots 1 to 8 are due to the different angular resolution of the original and the retrieved images and the sharp brightness temperature contrast in the coastlines (as in Fig. 6, right). In homogeneous scenes, such as when the ocean fills the extended AF-FOV (snap-shots 9 to 15), the rms errors are much smaller ~ 3 K, as predicted by the SMOS Error Budget [10].

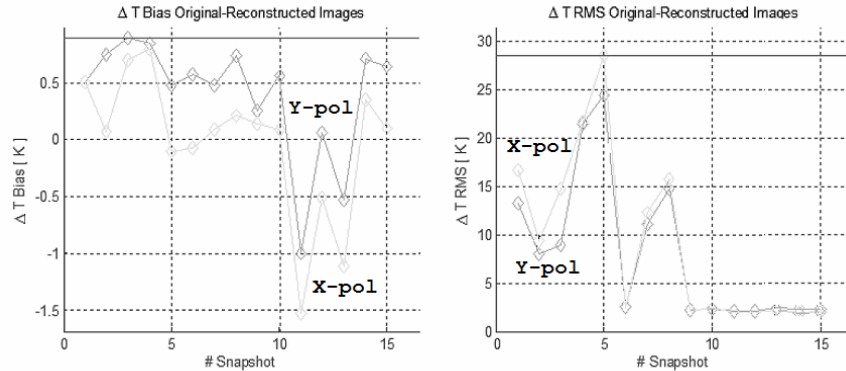


Figure 7. Bias (left) and rms error (right) at Y- (red) and X-pol (blue) for a series of 15 snap-shots.

V. CONCLUSIONS

The sources of the SDB have been investigated and have been found to be of two types:

- Contributors to $T_A = V(0,0)$: NIR measurement errors, contributions from the back of the array, and imperfect cancellation of Sun (and to much lesser extent Moon).
- Contributors to $V(u,v)$ (PMS and NIR measurement errors affecting the measurement of T_{sys} of each receiver (amplitude errors), differences between receivers' frequency responses (non-separable amplitude errors, and separable and non-separable phase errors), errors in the estimation of the antenna solid angle (amplitude errors), non-zero antenna cross-polarization patterns (leakage between T_B images from different polarizations: image-dependent offset term), and offsets.

The SDB can be minimized by reducing the T_B scene contrasts by adding all available information as proposed in previous versions of the image reconstruction algorithm, but also the land & iced-sea/sea mask and a reference ocean and a constant T_B over land to compute the differential visibilities to be inverted. Since the amplitude of the differential visibilities is smaller than the measured and calibrated visibilities, the same relative error leads to a smaller absolute error in the visibility samples and therefore, to a smaller bias.

The application of this technique allows imaging beyond the "alias free field of view" where the ocean alias overlaps with the land, and coastlines are much better defined. This result suggests that it could be possible to retrieve geophysical parameters closer to the coastlines and in the alias regions, although it is out of the scope of this work to analyze the performance the retrieval algorithms in these regions.



**IMAGE RECONSTRUCTION ALGORITHMS: UPDATE ON THE
ANALYSIS OF THE SCENE-DEPENDENT BIAS
SMOSP3-UPC-TN-0001 v 1.0**

Finally, by taking an HFFT of the resulting T_B image the Fourier components of the image can be directly obtained [5], for later post-processing with different windows for constant angular resolution (\bar{W} for all pixels) or for constant spatial resolution (strip-adaptive processing technique [22]).

ACKNOWLEDGMENTS

The work reported has been performed in the frame of the Spanish Research and EU Feder projects TEC2005-06863-C02-01/TCM and ESP2005-06823-C05-02.



REFERENCES

- [1] Kerr, Y.H.; Waldteufel, P.; Wigneron, J.-P.; Martinuzzi, J.; Font, J.; Berger, M.; Soil moisture retrieval from space: the Soil Moisture and Ocean Salinity (SMOS) mission, *IEEE Transactions on Geoscience and Remote Sensing*, Vol. 39 (8), pp. 1729 – 1735; August 2001
- [2] Font, J.; Lagerloef, G.S.E.; Le Vine, D.M.; Camps, A.; Zanife, O.-Z.; The determination of surface salinity with the European SMOS space mission, *IEEE Transactions on Geoscience and Remote Sensing*, Vol. 42 (10), pp. 2196-2205, October 2004
- [3] Corbella, I.; Duffo, N.; Vall-llossera, M.; Camps, A.; Torres, F., The visibility function in interferometric aperture synthesis radiometry, *IEEE Transactions on Geoscience and Remote Sensing*, Vol. 42 (8), pp. 1677 – 1682, August 2004
- [4] Camps, A., Ph. D. dissertation, Application of Interferometric Radiometry to Earth Observation, UPC, November 1996, <http://www.tdx.cesca.es/TDX-1020104-091741/>
- [5] Camps, A., J. Bará, I. Corbella, F. Torres, The Processing of Hexagonally Sampled Signals with Standard Rectangular Techniques: Application to 2D Large Aperture Synthesis Interferometric Radiometers, *IEEE Transactions on Geoscience and Remote Sensing*, Vol. 35, pp. 183-190, January 1997
- [6] Martin-Neira, M.; Ribo, S.; Martin-Polegre, A.J.; Polarimetric mode of MIRAS, *IEEE Transactions on Geoscience and Remote Sensing*, Vol. 40 (8), pp. 1755-1768, August 2002
- [7] Waldteufel, P., Kerr, Y., Boutin J., 2003, Selecting an optimal configuration for the Soil Moisture and Ocean Salinity mission *Radio Sci.*, Vol. 38, No. 3, 8051.
- [8] Camps, A., J. Bará, F. Torres, I. Corbella, Extension of the CLEAN Technique to the Microwave Imaging of Continuous Thermal Sources by Means of Aperture Synthesis Radiometers, *Progress In Electromagnetics Research*, PIER 18, pp. 67-83, January 1998
- [9] Camps, A., M. Vall.llossera, N. Duffo, F. Torres, I. Corbella, Retrieving Sea Surface Salinity With Multi-Angular L-band Brightness Temperatures: Improvement By Spatio-Temporal Averaging, *Radio Science*, Vol. 40, RS2003, doi:10.1029/2004RS003040, 2005, March 2005
- [10] Torres F., I. Corbella, A. Camps, N. Duffo, and M. Vall-llossera, Error budget map to SRD (PRS), ref. SO-TN-UPC-PLM-0007 v.7.0, Project Image validation support and SEPS development, validation and delivery for SMOS PLM, phase C/D, 14/02/2004
- [11] Torres, F., A. Camps, J. Bará, I. Corbella, R. Ferrero, On-Board Phase and Modulus Calibration of Large Aperture Synthesis Radiometers: Study Applied to MIRAS, *IEEE Transactions on Geoscience and Remote Sensing*, Vol. GRS-34, pp. 1000-1009, July 1996
- [12] Martin-Neira, M., S. Ribo, K. Rautiainen, 0-1 Correction of Comparator Threshold in 1-bit Interferometric Radiometers, *Proceedings of the 8th specialist Meeting on Microwave Radiometry and remote Sensing*



**IMAGE RECONSTRUCTION ALGORITHMS: UPDATE ON THE
ANALYSIS OF THE SCENE-DEPENDENT BIAS
SMOSP3-UPC-TN-0001 v 1.0**

- Applications, 24-27 February 2004, Faculty of Engineering, University "La Sapienza" of Rome, Rome, Italy.
- [13] Camps, A., F. Torres, J. Bará, I. Corbella, F. Monzón, Automatic calibration of channels frequency response in interferometric Radiometers, *Electronics Letters*, Vol. 35, No 2, pp. 115-116, 21 January 1999
- [14] Camps, A., I. Corbella, F. Torres, M. Vall-Ilossera, N. Duffo, Polarimetric formulation of the visibility function equation including cross-polar antenna patterns, *IEEE Geoscience and Remote Sensing, Letters*, Vol. 2 (3), pp. 292 – 295, July 2005
- [15] Camps, A., F. Torres, I. Corbella, N. Duffo, M. Vall-Ilossera, M. Martín-Neira. The impact of Antenna Pattern Frequency Dependence in Aperture Synthesis Microwave Radiometers, *IEEE Transactions on Geoscience and Remote Sensing*, Vol. 43(10), pp. 2218 – 2224, October 2005
- [16] Camps, A., M. Vall-Ilossera, N. Duffo, M. Zapata, I. Corbella, F. Torres, V. Barrena, Sun Effects In 2D Aperture Synthesis Radiometry Imaging And Their Cancellation, *IEEE Transactions on Geoscience and Remote Sensing*, Vol. 42 (6), pp. 1161-1167, June 2004
- [17] Camps, A., M. Vall-Ilossera, N. Reul, F. Torres, N. Duffo, I. Corbella, Impact and Compensation of Diffuse Sun Scattering in 2D Aperture Synthesis Radiometers Imagery, *Internacional Geoscience and Remote Sensing Symposium IGARSS 2005*, Seoul. Korea, 25-29 July 2005
- [18] Bará, J., A. Camps, F. Torres, and I. Corbella, Angular Resolution of two-dimensional hexagonally sampled interferometric radiometers, *Radio Science*, Vol. 33 (5), pp. 1459-1473, September-October 1998
- [19] Kopal, A., *The Moon*, ed. Reidel, Dordrecht, 1969.
- [20] Tanner A. B., and C. T. Swift, Calibration of a synthetic aperture radiometer *IEEE Transactions on Geoscience and Remote Sensing*, Vol. 31 (1), pp. 257 – 267, January 1993
- [21] Tomás Viver, R., "Algoritmos de reconstrucción de imagen en radiometría por síntesis de apertura," Final Project report, Advisors: N. Duffo and M. Vall-Ilossera, ETSETB / UPC, 2002
- [22] Ribó, S., Calibration Validation and Polarimetry in 2D Aperture Synthesis. Application to MIRAS, Ph. D. Thesis dissertation, Universitat Politècnica de Catalunya, 30-June-2005, Advisors: F. Torres, M. Martín-Neira, <http://www.tdx.cesca.es/TDX-0725105-154133/>

Appendix 1. Description of the Image Reconstruction Algorithm Proposed by UPC And Pre-processing of Visibility Samples

After the instrument internal calibration by uncorrelated/correlated noise injection [11] and 1/0 unbalance compensation [12] the system of equations to be solved is:

$$V_{12}^{pq}(u_{12}, v_{12}, w_{12}) = \frac{1}{\sqrt{\Omega_1 \Omega_2}} \iint_{\substack{\xi^2 + \eta^2 \leq 1 \\ \text{fore}}} \frac{T_{pq}(\xi, \eta) - T_{\text{rec}} \delta_{pq}}{\sqrt{1 - \xi^2 - \eta^2}} F_{np1}(\xi, \eta) F_{np2}^*(\xi, \eta) \tilde{r}_{12} \left(-\frac{u_{12}\xi + v_{12}\eta + w_{12}\sqrt{1 - \xi^2 - \eta^2}}{f_0} \right) \exp\left(-j2\pi \left(u_{12}\xi + v_{12}\eta + w_{12}\sqrt{1 - \xi^2 - \eta^2} \right)\right) d\xi d\eta, \quad (\text{A.1})$$

This equation includes the brightness temperature at pq polarization (T_{xx} , T_{yy} , or T_{xy} , being X and Y the antenna polarization axes), the Corbella term ($-T_{\text{rec}} \delta_{pq}$) [3], the product of the antenna voltage patterns ($F_{np1}(\xi, \eta) F_{np2}^*(\xi, \eta)$), the fringe-washing function (\tilde{r}_{12}) [13] and the errors in the baselines due to antenna positioning errors both in-plane and off-plane ($w_{12} \neq 0$). Contributions to the measured visibility samples from antenna backlobes are identical to eqn. (A.1) except for a sign change in w_{12} and appear as an offset term. In the case that the cross-polar patterns are taken into account, since the fourth Stokes parameter is negligible, the following substitutions had to be performed in (A.1) [3, 14]:

$$\begin{aligned} (T_{xx}(\xi, \eta) - T_{\text{rec}}) F_{nx1}(\xi, \eta) F_{nx2}^*(\xi, \eta) &\rightarrow R_{x1} R_{x2}^* (T_{xx} - T_{\text{rec}}) + (R_{x1} C_{x2}^* + C_{x1} R_{x2}^*) T_{yx} + C_{x1} C_{x2}^* (T_{yy} - T_{\text{rec}}), \\ (T_{yy}(\xi, \eta) - T_{\text{rec}}) F_{ny1}(\xi, \eta) F_{ny2}^*(\xi, \eta) &\rightarrow C_{y1} C_{y2}^* (T_{xx} - T_{\text{rec}}) + (R_{y1} C_{y2}^* + C_{y1} R_{y2}^*) T_{yx} + R_{y1} R_{y2}^* (T_{yy} - T_{\text{rec}}), \\ T_{yx}(\xi, \eta) F_{ny1}(\xi, \eta) F_{nx2}^*(\xi, \eta) &\rightarrow C_{y1} R_{x2}^* (T_{xx} - T_{\text{rec}}) + (R_{y1} R_{x2}^* + C_{y1} C_{x2}^*) T_{yx} + R_{y1} C_{x2}^* (T_{yy} - T_{\text{rec}}), \end{aligned} \quad (\text{A.2})$$

where $R_{p,n}$ ($\equiv F_{p,n}$) and $C_{p,n}$ are the co- and cross-polar patterns at p -polarization of the n^{th} antenna, and if the impact of the frequency dependence of the antenna patterns is not negligible and has to be taken into account, a simple way to do it is by replacing each antenna pattern products in (A.1) or (A.2) at the central frequency f_0 , by the following weighted average of the patterns at the central frequency (f_0) and the band edges ($f_0 \pm B/2$) [15]:

$$\frac{1}{4} F_{n1}(\xi, \eta, f_0 - B/2) F_{n2}^*(\xi, \eta, f_0 - B/2) + \frac{1}{2} F_{n1}(\xi, \eta, f_0) F_{n2}^*(\xi, \eta, f_0) + \frac{1}{4} F_{n1}(\xi, \eta, f_0 + B/2) F_{n2}^*(\xi, \eta, f_0 + B/2) \quad (\text{A.3})$$

As commented in section I, and first described in [4] and then refined in [8], a convenient way to perform the image reconstruction is by inverting a set of “differential visibilities” obtained from the calibrated ones by subtracting from them several terms:

- the sky visibilities, that allows one to extend the alias-free field of view (AF-FOV) to the replicas of the Earth horizon, instead of the replicas of the unit circle ($\xi^2 + \eta^2 = 1$), and
- a constant brightness temperature Earth term that reduces the Gibbs oscillations near the Earth replicas.

As described in [16, 17], the procedure can be readily extended to account for other terms such as the direct and scattered Sun and Moon contributions, the Corbella term, and the contribution from the antenna back lobes. This procedure is formally described below.

A. AF-FOV Extension

AF-FOV extension up to the Earth replicas is performed by subtracting from the visibility samples the following contributions (“auxiliary visibilities”) computed from the measured antenna patterns and the estimated fringe-wash function [13]:

- the Corbella term due to the receivers’ physical temperature ($-T_{rec}$). This term appears as an offset in all the visibility samples [3] except at the zero baseline (the antenna temperature, which is measured by three dedicated NIRs (eqn. (A.5)).

$$V_R^{pq} \stackrel{\Delta}{=} \frac{1}{\sqrt{\Omega_1 \Omega_2}} \iint_{\xi^2 + \eta^2 \leq 1} \frac{-T_{rec}}{\sqrt{1 - \xi^2 - \eta^2}} \hat{F}_{n1}^p(\xi, \eta) \hat{F}_{n2}^{q*}(\xi, \eta) \hat{r}_{12} \left(-\frac{u_{12}\xi + v_{12}\eta + w_{12}\sqrt{1 - \xi^2 - \eta^2}}{f_0} \right) \exp\left(-j2\pi(u_{12}\xi + v_{12}\eta + w_{12}\sqrt{1 - \xi^2 - \eta^2})\right) d\xi d\eta, \quad (A.4)$$

$$\bar{T}_A^{pq} = V^{pq}(0, 0) = \sum_{\forall m} T_{A,m,m}^{pq} / 3, \quad (A.5)$$

- the sky visibilities:

$$V_{sky}^{pq} \stackrel{\Delta}{=} \frac{1}{\sqrt{\Omega_1 \Omega_2}} \iint_{\xi^2 + \eta^2 <_{sky}} \frac{T_{B,sky}^{pq}(\xi, \eta)}{\sqrt{1 - \xi^2 - \eta^2}} \hat{F}_{n1}^p(\xi, \eta) \hat{F}_{n2}^{q*}(\xi, \eta) \hat{r}_{12} \left(-\frac{u_{12}\xi + v_{12}\eta + w_{12}\sqrt{1 - \xi^2 - \eta^2}}{f_0} \right) \exp\left(-j2\pi(u_{12}\xi + v_{12}\eta + w_{12}\sqrt{1 - \xi^2 - \eta^2})\right) d\xi d\eta, \quad (A.6)$$

- the visibilities measured by the antenna back lobes (note that there are two-directions in the space $(\xi, \eta, +\sqrt{1 - \xi^2 - \eta^2})$ and $(\xi, \eta, -\sqrt{1 - \xi^2 - \eta^2})$ corresponding to the same (ξ, η) point being imaged)

$$V_{12}^{pq} \Big|_{\text{back}} = \frac{1}{\sqrt{\Omega_1 \Omega_2}} \iint_{\xi^2 + \eta^2 \leq 1} \frac{T_{pq, \text{back}}(\xi, \eta) - T_{\text{rec}} \delta_{pq}}{\sqrt{1 - \xi^2 - \eta^2}} \hat{F}_{np1}(\xi, \eta) \hat{F}_{np2}(\xi, \eta) \hat{r}_{12} \left(-\frac{u_{12}\xi + v_{12}\eta - w_{12}\sqrt{1 - \xi^2 - \eta^2}}{f_0} \right) \exp\left(-j2\pi\left(u_{12}\xi + v_{12}\eta - w_{12}\sqrt{1 - \xi^2 - \eta^2}\right)\right) d\xi d\eta. \quad (\text{A.7})$$

Note the sign change before w_{12} , as compared to the visibilities corresponding to the fore lobe.

B. Cancellation of Sun and Moon effects

The Sun and the Moon appear in the sky region of the brightness temperature images, since they are extended up to the periodic repetition of the Earth-sky horizon. Since the brightness temperature of the Sun at L-band is very high (between ~ 100.000 and $\sim 1.000.000$ K), highly variable in time and polarization-dependent, it is necessary to estimate its value preferably from the data itself. The procedure to do so is described in [16] and consists of the following steps:

- First a “raw” brightness temperature image by taking the inverse hexagonal Fourier transform of:

$$\hat{T}_B^{pq} = \mathcal{F}^{-1} \left[V^{pq}(u, v) - V_R^{pq}(u, v) \right]. \quad (\text{A.8})$$

Since the Sun is such a bright source it appears as a very bright pixel. Its location in the $(\xi_{Sun, dir}, \eta_{Sun, dir})$ plane can be inferred from it, or it can be computed from the date and the platform position and attitude.

- The instrument’s response for a 1 K amplitude point-source is computed in the direction of the brightest pixel in eqn. (11).

$$\hat{T}_{Sun, dir}^{pq} = \mathcal{F}^{-1} \left[\bar{V}_{Sun, dir}^{pq}(u, v) \right]. \quad (\text{A.9})$$

- Subtracting from eqn. (A.9) an average brightness temperature from the sea or the land at the Sun’s position $(\xi_{Sun, dir}, \eta_{Sun, dir})$, the brightness temperature of Sun can be estimated as:

$$T_{Sun, dir}^{pq} = \hat{T}_B^{pq}(\xi_{Sun, dir}, \eta_{Sun, dir}) / \hat{T}_{Sun, dir}^{pq}(\xi_{Sun, dir}, \eta_{Sun, dir}). \quad (\text{A.10})$$

- Finally, the non-normalized visibilities corresponding to the Sun can be estimated from eqn. (A.10) and the antenna patterns measured on ground used to compute $\bar{V}_{Sun, dir}^{pq}(u, v)$:

$$V_{Sun, dir}^{pq}(u, v) = T_{Sun, dir}^{pq} \cdot \bar{V}_{Sun, dir}^{pq}(u, v). \quad (\text{A.11})$$

- For the scattered Sun a similar procedure can be applied, but using an appropriate scattering model over the sea or over the land with the necessary auxiliary data (e.g. salinity, temperature, and wind speed, or soil surface temperature, moisture, roughness, and vegetation opacity and albedo):

$$V_{Sun, scatt}^{pq}(u, v) = T_{Sun, dir}^{pq} \cdot \bar{V}_{Sun, scatt}^{pq}(u, v). \quad (\text{A.12})$$

However, since the scattered contribution appears always in the aliased region, its impact in the AF-FOV is very small and only due to the spill over from the alias regions into the AF-FOV due to the finite angular resolution [18].

- The self-estimation technique cannot be applied to the Moon since, because of its much lower brightness temperature, there is no clear peak in the brightness temperature images. However, a constant 250 K value can be used [19] and applied. The Moon's contribution to the antenna temperature is negligible, about $250 K (0.5^\circ/60^\circ)^2 = 0.02 K$ if it were located in the antenna boresight.

C. Computation of the Differential Visibilities

The computation of the differential visibilities is the key step not only of the mitigation of the SDB and it is described in eqns. 4 to 7, but also of the cancellation of the Sun effects...

D. Image Reconstruction Techniques

Finally, the system of equations to be inverted has the form:

$$\Delta V^{pq} \stackrel{\Delta}{=} \frac{1}{\sqrt{\Omega_1 \Omega_2}} \iint_{\xi^2 + \eta^2 < Earth} \frac{\Delta T_B^{pq}(\xi, \eta)}{\sqrt{1 - \xi^2 - \eta^2}} \hat{F}_{n1}^p(\xi, \eta) \hat{F}_{n2}^{q*}(\xi, \eta) \hat{r}_{12} \left(\frac{u_{12}\xi + v_{12}\eta + w_{12}\sqrt{1 - \xi^2 - \eta^2}}{f_0} \right) \exp\left(-j2\pi(u_{12}\xi + v_{12}\eta + w_{12}\sqrt{1 - \xi^2 - \eta^2})\right) d\xi d\eta, \quad (A.13)$$

which can be written for all baselines in a matrix form:

$$\overline{\Delta V} = \overline{\overline{G}} \cdot \overline{\Delta T}^{dec}, \quad (A.14)$$

where $\overline{\overline{G}}$ is the matrix that describes the instrument's response for a point source in each direction, and $\overline{\Delta T}^{dec}$ is the differential T_B being imaged. Equation (A.14) can be solved directly (if feasible in large interferometric radiometers) by the Moore-Penrose Pseudo-inverse [20], by a SVD, or by a conjugate-gradient method, or using linear algebra methods after stabilization by pre-multiplication by the hermitian of the $\overline{\overline{G}}$ matrix ($\overline{\overline{G}}^H$), the normal equation $\overline{\overline{G}}^H \cdot \overline{\Delta V} = \overline{\overline{G}}^H \cdot \overline{\overline{G}} \cdot \overline{\Delta T}^{dec}$. The current implementation in the SMOS End-to-end Performance Simulator, SEPS, solves the normal equation by the conjugate-gradient so that it can be executed in most PCs [21]. In solving eqn. (A.14) it is most convenient to sample the (ξ, η) points in the reciprocal grid of the (u, v) one to improve the condition number of $\overline{\overline{G}}$ and to allow the use of FFTs over hexagonal grids [5]. Note also that in the ideal case, and when the number of baselines is equal to the number



**IMAGE RECONSTRUCTION ALGORITHMS: UPDATE ON THE
ANALYSIS OF THE SCENE-DEPENDENT BIAS
SMOSP3-UPC-TN-0001 v 1.0**

of imaged pixels, $\overline{\overline{G}}$ is equal to the Fourier matrix $\overline{\overline{F}}$, then $\overline{\overline{F}}^{-1} = \overline{\overline{F}}^H$ and $\overline{\overline{\Delta T}}^{dec} = \overline{\overline{F}}^{-1} \cdot \overline{\overline{F}} \cdot \overline{\overline{\Delta T}}^{dec} = \overline{\overline{F}}^{-1} \cdot \overline{\overline{\Delta V}}$ as expected.

Finally, the brightness temperature map is formed by adding the ΔT , the sea and the land/iced sea contributions:

$$T_B^{\rho q}(\xi, \eta) \triangleq \Delta T_B^{\rho q}(\xi, \eta) + T_{sea}^{\rho q}(\xi, \eta) + T_{land}^{\rho q} \cdot land(\xi, \eta) \quad , \quad (A.15)$$

where $land(\xi, \eta)$ is a function that defines the (ξ, η) region occupied by land or iced sea.